

# <sup>10</sup>B-doped MCP detector developed for neutron resonance imaging at Back-n white neutron source\*

Qiang Li,<sup>1,2,3</sup> Li-Jiao Wang,<sup>1,2,4,†</sup> Jing-Yu Tang,<sup>5,6,‡</sup> Xiang-Biao Qiu,<sup>7</sup> Zhen Chen,<sup>6,8</sup> Mao-Yuan Zhao,<sup>6,8</sup> Chang-Jun Ning,<sup>1,2</sup> Kai Pan,<sup>7</sup> Wei Xu,<sup>7</sup> Tao Li,<sup>7</sup> Su-Peng Lu,<sup>1,2</sup> Han Yi,<sup>1,2</sup> Rui-Rui Fan,<sup>1,2,3</sup> Chang-Qing Feng,<sup>6,8</sup> Rong Zhang,<sup>7</sup> Xiao-Yang Sun,<sup>1,2</sup> Qi An,<sup>6,8</sup> Hao-Fan Bai,<sup>9</sup> Jiang-Bo Bai,<sup>10</sup> Jie Bao,<sup>11</sup> Ping Cao,<sup>5,6</sup> Qi-Ping Chen,<sup>12</sup> Yong-Hao Chen,<sup>1,2</sup> Zeng-Qi Cui,<sup>9</sup> An-Chuan Fan,<sup>13</sup> Fan-Zhen Feng,<sup>13</sup> Min-Hao Gu,<sup>1,3</sup> Chang-Cai Han,<sup>14</sup> Zi-Jie Han,<sup>12</sup> Guo-Zhu He,<sup>11</sup> Yong-Cheng He,<sup>1,2</sup> Yang Hong,<sup>1,2,15</sup> Yi-Wei Hu,<sup>9</sup> Han-Xiong Huang,<sup>11</sup> Wei Jiang,<sup>1,2</sup> Zhi-Jie Jiang,<sup>6,8</sup> Zheng-Yao Jin,<sup>13</sup> Ling Kang,<sup>1,2</sup> Bo Li,<sup>1,2</sup> Gong Li,<sup>13</sup> Xiao Li,<sup>1,2</sup> Yang Li,<sup>1,2</sup> Jie Liu,<sup>9</sup> Rong Liu,<sup>12</sup> Shu-Bin Liu,<sup>6,8</sup> Yi-Na Liu,<sup>11</sup> Guang-Yuan Luan,<sup>11</sup> Jie Ren,<sup>11</sup> Zhi-Zhou Ren,<sup>12</sup> Xi-Chao Ruan,<sup>11</sup> Zhao-Hui Song,<sup>14</sup> Kang Sun,<sup>1,2</sup> Zhi-Xin Tan,<sup>1,2</sup> Sheng-Da Tang,<sup>1,2</sup> Jin-Cheng Wang,<sup>11</sup> Peng-Cheng Wang,<sup>1,2</sup> Zhao-Hui Wang,<sup>11</sup> Zhong-Wei Wen,<sup>12</sup> Xiao-Guang Wu,<sup>11</sup> Xuan Wu,<sup>1,2</sup> Cong Xia,<sup>9</sup> Yong-Ji Yu,<sup>1,2</sup> Guo-Hui Zhang,<sup>9</sup> Hang-Chang Zhang,<sup>1</sup> Lin-Hao Zhang,<sup>1,2</sup> Qi-Wei Zhang,<sup>11</sup> Xian-Peng Zhang,<sup>14</sup> Yu-Liang Zhang,<sup>1,2</sup> Yue Zhang,<sup>1,2</sup> Zhi-Yong Zhang,<sup>6,8</sup> Zhi-Hao Zhou,<sup>1,2,15</sup> Ke-Jun Zhu,<sup>1,3,15</sup> and Chong Zou<sup>11,16</sup>

<sup>1</sup>*Institute of High Energy Physics, Chinese Academy of Sciences (CAS), Beijing 100049, China*

<sup>2</sup>*Spallation Neutron Source Science Center, Dongguan 523803, China*

<sup>3</sup>*State Key Laboratory of Particle Detection and Electronics,*

*Institute of High Energy Physics Chinese Academy of Sciences, Beijing 100049, China*

<sup>4</sup>*Dongguan Songshan Lake Future School, Dongguan 523808, China*

<sup>5</sup>*School of Nuclear Science and Technology, University of Science and Technology of China, Hefei 230027, China*

<sup>6</sup>*State Key Laboratory of Particle Detection and Electronics,*

*University of Science and Technology of China, Hefei 230026, China*

<sup>7</sup>*North Night Vision Science & Technology (Nanjing) Research Institute Co. Ltd., Nanjing 211106, China*

<sup>8</sup>*Department of Modern Physics, University of Science and Technology of China, Hefei 230026, China*

<sup>9</sup>*State Key Laboratory of Nuclear Physics and Technology,*

*School of Physics, Peking University, Beijing 100871, China*

<sup>10</sup>*Institute of Modern Physics, Fudan University, Shanghai 200433, China*

<sup>11</sup>*Key Laboratory of Nuclear Data, China Institute of Atomic Energy, Beijing 102413, China*

<sup>12</sup>*Institute of Nuclear Physics and Chemistry, China Academy of Engineering Physics, Mianyang 621900, China*

<sup>13</sup>*USTC archaeometry lab, University of Science and Technology of China, Hefei 230026, China*

<sup>14</sup>*Northwest Institute of Nuclear Technology, Xi'an 710024, China*

<sup>15</sup>*University of Chinese Academy of Sciences, Beijing 100049, China*

<sup>16</sup>*China Shipbuilding Trading Co., Ltd., Beijing 100044, China*

Neutron resonance imaging (NRI) has recently emerged as an appealing technique for neutron radiography. Its complexity surpasses that of conventional transmission imaging, as it requires a high demand for both a neutron source and detector. Consequently, the progression of NRI technology has been sluggish since its inception in the 1980s, particularly considering the limited studies analyzing the neutron energy range above keV. The white neutron source (Back-n) at the China Spallation Neutron Source (CSNS) provides favorable beam conditions for the development of the NRI technique over a wide neutron energy range from eV to MeV. Neutron-sensitive microchannel plates (MCP) have emerged as a cutting-edge tool in the field of neutron detection owing to their high temporal and spatial resolutions, high detection efficiency, and low noise. In this study, we report the development of a <sup>10</sup>B-doped MCP detector, along with its associated electronics, data processing system, and NRI experiments at the Back-n. Individual heavy elements such as gold, silver, tungsten, and indium can be easily identified in the transmission images by their characteristic resonance peaks in the 1-100 eV energy range; the more difficult medium-weight elements such as iron, copper, and aluminum with resonance peaks in the 1-100 keV energy range can also be identified. In particular, results in the neutron energy range of dozens of keV (Aluminum) are reported here for the first time.

Keywords: Neutron resonance imaging; <sup>10</sup>B doped MCP detector; White neutron source; Sample nuclide identification

## I. INTRODUCTION

Neutron resonance imaging (NRI) is a nondestructive technique for detecting the nuclide composition and distribution in samples [1–4]. Compared with traditional X-ray and neutron transmission imaging, it has the advantages of nuclide identification and can provide more comprehensive information regarding the samples. NRI has broad application prospects in materials, archaeology, the nuclear industry, and other fields [5–9]. This technique aims to analyze the nu-

\* This work was supported by the National Natural Science Foundation of China (Project 12035017) and the Guangdong Basic and Applied Basic Research Foundation (No.2023A1515030074).

† Corresponding author, wanglj@ihep.ac.cn(Li-Jiao Wang)

‡ Corresponding author, jytang@ustc.edu.cn(Jing-Yu Tang)

clide composition and distribution in samples by using the characteristic resonances of neutron interactions. Imaging quality heavily relies on the neutron source and the performance of the neutron detector. Specifically, the detector is expected to achieve high temporal and spatial resolutions, a wide response range of the neutron energy, and a high detection efficiency to obtain the energy-counting rate spectrum at each spatial pixel. A neutron source must have a wide energy spectrum, high flux, and good temporal resolution. Therefore, the NRI technique presents greater challenges, particularly for medium-energy neutrons ranging from hundreds of eV to hundreds of keV. Current neutron detectors have a low detection efficiency in this energy range, which complicates developing NRI to cover light to heavy elements.

Many neutron-detector types, such as scintillator arrays, multi-pole photomultipliers, and position-sensitive gas detectors, are limited by their detection efficiency and spatial resolution, thus cannot fully meet the requirements of NRI [10–14]. CCD/CMOS cameras with gated time windows have been used in NRI to identify nuclides with resonance peaks in the eV energy range [15–17]. However, their low detection efficiency and poor signal-to-noise ratio hinder attaining favorable results above the keV range. Neutron-sensitive microchannel plates (nMCPs) have excellent properties including good temporal and spatial resolutions, irradiation resistance, a high gain, and low noise. They have been developed for general neutron imaging, including thermal neutron imaging, and are considered suitable for the NRI technique owing to their potential for a high neutron detection efficiency [18, 19]. The most commonly used nMCPs are Boron- and Cadmium-doped detectors. The nMCP matched with Timepix3 electronics has been used in NRI and demonstrated a good performance in the ultra-thermal neutron energy region [20–24]. However, it is difficult to identify nuclides with resonances above the keV range. As an analog-digital hybrid chip, the irradiation resistance of Timepix3 is affected by high-flux neutron sources. A suitable neutron source with a good time resolution and high flux covering a large energy range is rarely found. The white neutron source (Back-n) at the China Spallation Neutron Source (CSNS) was built in 2018 and serves as a multi-purpose platform to support nuclear data measurements, detector calibrations, and irradiation-effect tests [25–28]. Back-n exhibits the advantages of a wide energy spectrum (0.5 eV–200 MeV), high flux ( $2 \times 10^7$  n/cm<sup>2</sup>/s at 55 m from the target with  $\Phi 60$  mm spot), low background, and good temporal resolution (<1%), which provide favorable beam conditions for exploiting the NRI technique over a wide neutron energy range from eV to MeV [29–32].

This study reports the development of a <sup>10</sup>B-doped MCP (called B-MCP hereafter) detector system that includes crossed anode strips, readout electronics, and data processing. Anode strips are suitable for NRI owing to their good performance in terms of the irradiation resistance, spatial resolution (100  $\mu$ m), and counting rate (10 MHz/cm<sup>2</sup>). Several NRI demonstration experiments were conducted at Back-n to identify various elements with resonances in different energy regions, ranging from eV to dozens of keV, the performance

of which exceeded that reported in literature.

## II. EXPERIMENTAL SETUP

The detector system mainly consisted of a B-MCP/MCP stack, crossed anode strips, a front-amplifier module (FAM), a vacuum chamber, readout electronics (including digitization modules (FDMs) and a data aggregation module (DAM)), and a data acquisition computer, as shown in Fig. 1.

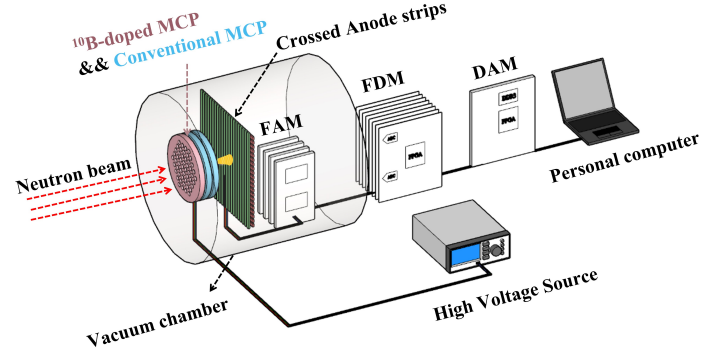


Fig. 1. Schematic of the B-MCP detector system.

The B-MCP/MCP stack, as the core part of the detector, was composed of one B-MCP and two conventional MCPs encapsulated in a ceramic fixture. The B-MCP was developed in cooperation with North Night Vision, and its main parameters are listed in Table 1. It contained approximately 10 mol% <sup>10</sup>B, which was owing to glass substrate doping, and the signal gain was approximately one order of magnitude lower than that of the conventional MCP, which is beneficial for neutron detection. A large gain in the B-MCP leads to an excessive amplitude range of neutron signals, which is not conducive to the efficient acquisition of neutron events by specific electronics. The MCP pores had a bevel angle of approximately 8° and were stacked in a V-shape of two adjacent MCPs to improve the secondary electron efficiency and reduce ion feedback. The voltage ratio of the B-MCP and the MCPs was 2:3:3 to further reduce the B-MCP gain, that is, the neutron signal amplitude range.

Table 1. Main parameters of the B-MCP and a conventional MCP.

Parameters	B-MCP	Conventional MCP
Diameter(mm)	56	56
Thickness(mm)	0.51	0.48
Body resistance(M $\Omega$ )	42	46
Pore inner diameter( $\mu$ m)	8	10
Pore area ratio (%)	60	60
Gain@800V	120	2800
<sup>10</sup> B (mol%)	10	—

The  $\alpha$  or <sup>7</sup>Li produced from the nuclear reaction of <sup>10</sup>B(n,  $\alpha$ )<sup>7</sup>Li with an incident neutron that can penetrate the substrate enters one or more pores of the B-MCP and excites

the primary electrons on the inner wall. The electrons multiply many times in the pores to form an electron cloud at the exit surface of the MCP and were collected by the crossed anode strips to form the primary signal of the neutron case. The crossed strips consisted of diamond pads distributed on the surface layer of the PCB board. The pads were interleaved in both the X- and Y-directions, forming a sensitive area of  $65 \times 65 \text{ mm}^2$  with a total of 256 channels (the X- and Y-directions were both 128 channels). The strip pitch in both directions was 0.508 mm with a 0.10 mm gap between adjacent pads. A schematic of this structure is shown in Fig. 2a. The gap between the exit surface of the MCP and the layer of the strips was 1.1 mm, allowing the electron cloud to "fire" multiple adjacent strips to facilitate the localization of the neutron case.

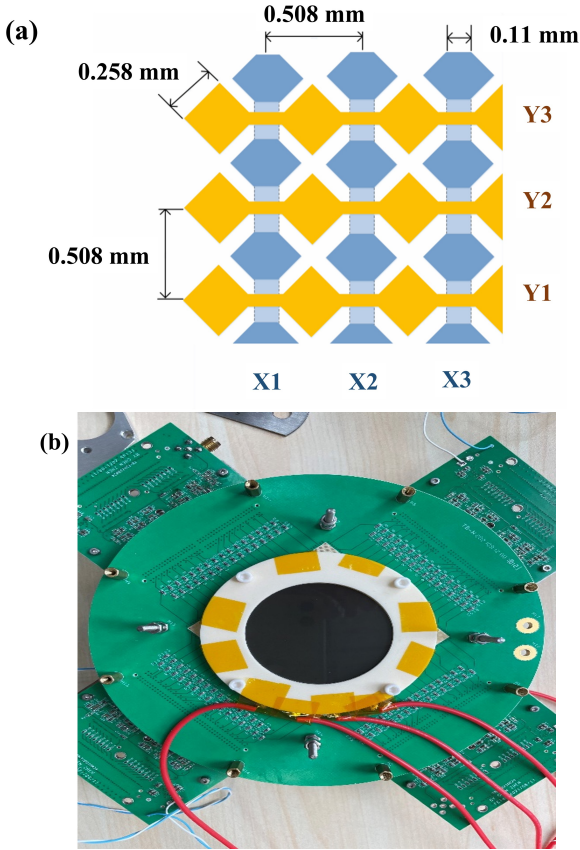


Fig. 2. (a) Local schematic structure of the crossed anode strips [33]; (b) physical object of the FAMS packed with the B-MCP/MCP stack.

Primary signals were amplified and filtered by the FAMS before further processing, and the FAMS were packed with a B-MCP stack inside a vacuum chamber to avoid noise. The physical objects of the package are shown in Fig. 2b. The electronics system was developed in collaboration with the University of Science and Technology of China (USTC). Eight FDM boards outside the chamber were responsible for the waveform digitization of the amplified signals. The sampling frequency was set to 80 MHz to accommodate a signal pulse width of  $\sim 700 \text{ ns}$ . The data were aggregated onto a

DAM board for storage and offline analysis. The electronics system was triggered by a T0 signal from a proton beam monitor (a fast current transformer FCT on the accelerator) as the starting time of the neutron flight, and the threshold was set to 50 fC to filter the noise of the electronics and wait for the signal trigger. The sampling duration was set to  $0.6 \mu\text{s}$  before and  $1.0 \mu\text{s}$  after the signal trigger, and the waveform on each strip was recorded.

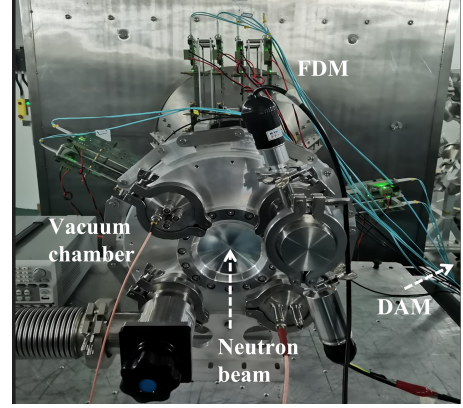


Fig. 3. Experimental layout of the detector at the Back-n white neutron source.

The experimental layout of the B-MCP detector at the Back-n white neutron source is shown in Fig. 3. Eight FDM boards were assembled in the chamber to optimize space-utilization and avoid direct beam irradiation. The surface of the B-MCP was approximately 76 m distant from the spallation target. The beam spot at the detector was  $\Phi 30 \text{ mm}$ , which was smaller than the diameter of the B-MCP, allowing the neutron beam to completely pass through the sensitive area of the detector. The neutron flux was approximately  $8.5 \times 10^5 \text{ n/cm}^2/\text{s}$ , and the energy range was 0.5 eV-200 MeV [34]. The neutron pulse repetition rate was 25 Hz and had a double-bunch structure with an interval of 410 ns and a width of 60 ns for each bunch. This introduced an error of more than 10% in the temporal resolution of neutrons above the MeV range, whereas for neutrons below dozens of keV, this effect was less than 1% and could be ignored in the experiments.

### III. EXPERIMENT PROCESS AND DATA ANALYSIS METHOD

An empty period of  $6 \mu\text{s}$  after the T0 trigger was set to avoid data blocking in the electronic channels owing to the complex responses of MCP components to the high-energy neutrons. Accordingly, the available energy ranged from 0.5 eV to approximately 0.5 MeV. The amplitude spectra of the MCP dark counts and neutron signals were measured by increasing the voltage on the MCPs. Both the amplitudes of the dark count and neutron signal increased, and the two spectra gradually separated as the voltage increased. An appropriate voltage of 2400 V was selected to obtain a good neutron/dark count ratio, as shown in Fig. 4. Certain large neutron signals



were saturated at an ADC channel of approximately 3500 owing to the limitation of the electronics dynamic range. Conversely, certain small signals were mixed in the dark counts and were difficult to separate. This is because the neutron signals have a significantly wide amplitude range owing to the B-MCP gain. We set a second threshold at an ADC channel of approximately 900 to exclude the dark counts and noise. Certain small signals, whose amplitudes cannot be separated from the dark counts, will inevitably be lost. This reduces the overall detection efficiency, but does not affect the trend and details of the neutron spectrum because the amplitude of the neutron signal with an energy below a few hundred keV is nearly independent of the neutron energy.

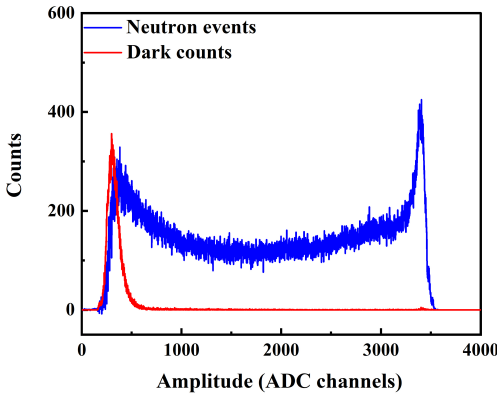


Fig. 4. Amplitude spectra of the neutron cases and MCP dark counts at a voltage of 2400 V.

Multiple adjacent channels are typically fired on the X and Y strips at each neutron event; a typical signal is shown in Fig. 5. Normally, the signal amplitude in the middle channel is higher than those on both sides, conforming to the electron cloud distribution. A data analysis extracts the time-of-flight and hit positions of each neutron to plot the neutron energy spectrum and beam spot image. The stop time of the neutron flight is obtained using the peak of the unsaturated channels because the peak position has a stable amplitude; furthermore, unsaturated channels are always present, even for the saturated case. Peak deviations of more than two sampling points (approximately 25 ns) are considered different events within a sampling window, although these situations are significantly rare in the energy region below hundreds of keV. Both gravity and the center of the electron cloud distribution can provide a spatial resolution of better than 100  $\mu\text{m}$ , which exceeds the width limit of the anode strips. However, this significantly reduces the counts on each pixel and is not conducive to the neutron spectrum analysis for resonance imaging. Because the present efficiency of B-MCP is not sufficiently high, we used the central anode strip of the response strips in both the X and Y directions as the hitting point with a spatial resolution of 500  $\mu\text{m}$  depending on the pitch of the anode strips.

Fig. 6a presents the neutron energy-count spectrum measured on the Back-n source for 7200 s after deducting the

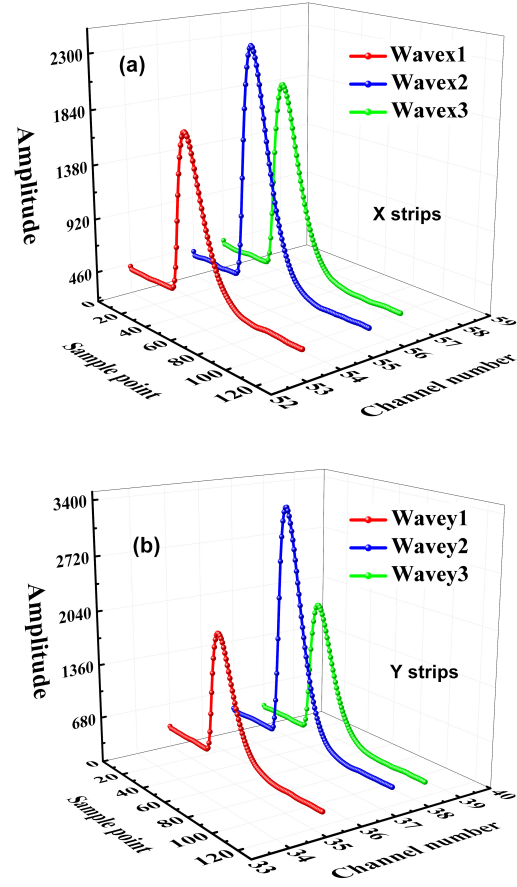


Fig. 5. Waveform of a typical neutron signal in the (a) X and (b) Y directions.

dark counts and noise. The kinetic energy of neutrons can be calculated using Eq. (1).

$$E_n = (\gamma - 1)m_n c^2$$

$$\gamma = \frac{1}{\sqrt{1 - (v/c)^2}} \quad (1)$$

where  $v = L_{flight}/TOF$ . The neutron flight length  $L_{flight}$  is 76 m from the neutron target to the surface of the B-MCP. The curve in Fig. 6a shows the response spectrum of the  $^{10}\text{B}$  doped in the B-MCP at the Back-n source. Numerous detailed peaks ranging from 0.5 eV to tens of keV arise from the intrinsic microstructure of the Back-n energy spectrum. The resonance peaks of certain nuclides such as  $^{181}\text{Ta}$  (~4.2 eV),  $^{95}\text{Mo}$  (~45 eV),  $^{55}\text{Mn}$  (~340 eV), and  $^{56}\text{Fe}$  (~28 keV) in the spallation target are marked. Fig. 6b presents the Back-n beam spot image measured by the B-MCP detector. The half-height, full-width profile of the image was fitted to a diameter of approximately 30 mm, which coincided with the beamline setting. The outer profile of the image corresponds to the size of the B-MCP, that is 56 mm in diameter. The energy spectrum and beam spot of the neutron source can be simultaneously obtained in a single measurement using a



B-MCP detector. Moreover, with a sufficiently high detection efficiency (or total counts), a more detailed analysis can be performed on the energy spectra in different spot areas or beam spots at different energy intervals. Here, the neutron energy-count spectrum and beam spot of Back-n is demonstrated to provide a comparison of the data for the neutron resonance imaging experiments with the samples presented in Sec. IV.

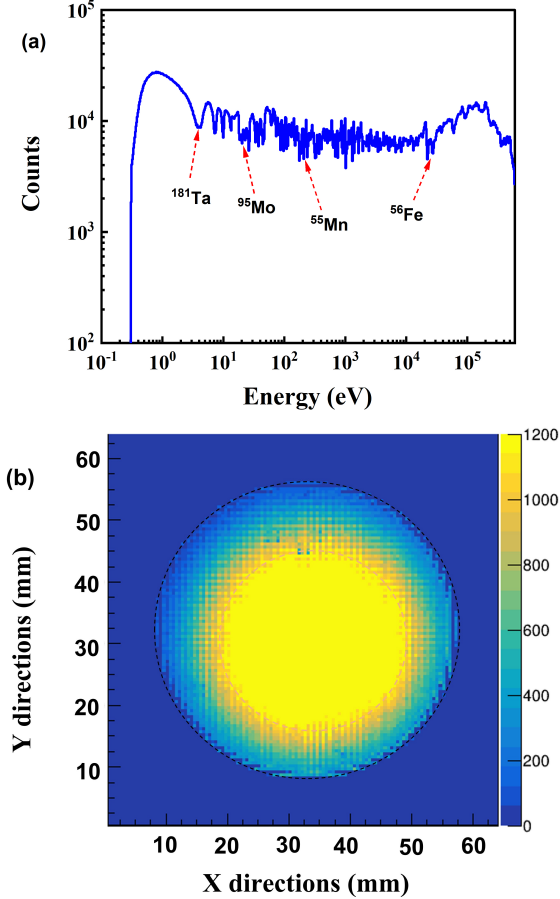


Fig. 6. Neutron energy-count spectrum and (a) beam spot of the Back-n source (b) measured by the B-MCP detector. The identified image is distinctive by a yellow-blue scale.

#### IV. NRI EXPERIMENTS

The B-MCP detector can provide the position and energy information of each neutron case, such that the data can be flexibly processed in resonance imaging experiments to efficiently obtain more valuable information. In this section, the heavy elements including In, Au, Ag, and W with resonances in the eV energy region and the medium-mass elements including Cu, Fe, and Al with resonances in the keV energy region were selected to study the resonance imaging effect of the B-MCP detector on the Back-n source. For a sam-

ple with an unknown composition, there are two approaches for determining the nuclides and their distribution in the sample: 1) Comparison of the neutron energy-count spectra in the full image with and without a sample to determine the nuclide components; the neutrons in the resonance region were then selected for imaging to obtain the spatial distribution of the corresponding nuclide. 2) Observing the sample distribution using the total neutron transmission imaging; the neutron energy-count spectra at the sample locations were then analyzed for the nuclide composition. A combination of these two methods allowed for a significantly adequate compositional analysis of the samples. In particular, for a small number of nuclides in a sample, the latter is more effective.

##### A. Nuclides with cross-section resonances in the 1-100 eV regions

In the eV-energy region, four typical elements including Au, Ag, In, and W were selected, and their dominant cross-sectional resonances [35] with natural abundances are shown in Fig. 7. These resonances are distributed in the energy range of 1-100 eV, in which the cross-sections of  $^{197}\text{Au}$  and  $^{115}\text{In}$  were approximately 30,000 barns, and the cross-sections of  $^{nat}\text{Ag}$  and  $^{nat}\text{W}$  were approximately 10000 barns, indicating a strong resonance absorption of neutrons in this region. In addition, the B-MCP detector has a relatively high detection efficiency in this region owing to the larger cross-section of  $^{10}\text{B}$ , which is approximately a few hundred barns. Therefore, the identification and imaging of these nuclides in this energy region are relatively easy.

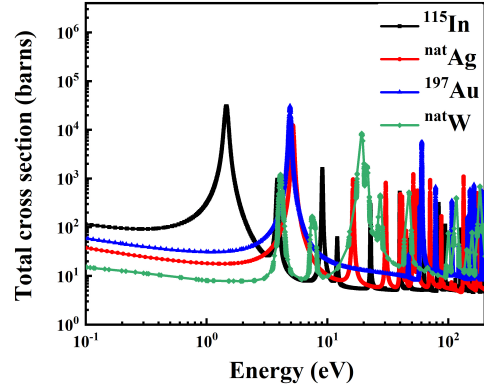


Fig. 7. Cross-sections of  $^{115}\text{In}$ ,  $^{nat}\text{W}$ ,  $^{197}\text{Au}$ , and  $^{nat}\text{Ag}$  within the energy region of 1-200 eV.

Fig. 8a presents the objects of the four samples in different shapes with the same thickness of 1.0 mm. These samples were placed at the center of the neutron beam, 70 mm distant from the B-MCP detector, such that the neutrons vertically passed through the sample plane. Using the aforementioned experimental conditions, the measurement was performed for 3 h and the total-transmission imaging of the samples was obtained, as shown in Fig. 8b. Initially, we compared the

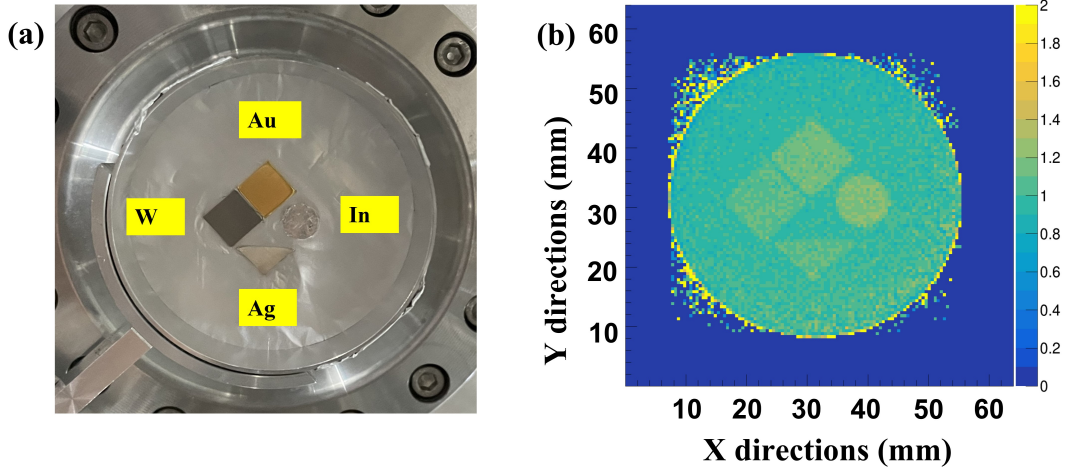


Fig. 8. (a) Sample objects and (b) the neutron transmission image over the full-energy region.

total neutron energy-count spectra with and without these samples. The results show no apparent difference between these two spectra, and the strong resonance absorptions are invisible (the two identical spectra are the same as those in Fig. 6a, implying that the nuclide composition cannot be determined first. The number of these samples was relatively small, and the large amount of data in the sample-free region served as a background to extract the resonance peaks of the samples. However, in the total-transmission images, the profiles of the four samples were clearly visible. The image underwent background subtraction and was normalized to the comparison data without the samples. The brightness reflects the intensity of neutron absorption, that is, the amount of the sample. It is impossible to identify the sample components in the total-transmission image without their shapes because the brightness value is related to both the cross-sections of the nuclides and their areal density on the pixels.

We selected the neutron energy-count spectra from the sample areas and normalized them to the comparison data to obtain the ratio spectra with and without the samples, as shown in the ratio spectra in Fig. 9. The peak clusters in the ratio spectra reflect the nuclide species, and the intensity of the peaks reflects the areal density of the nuclides, which sufficiently corresponds with the primary and secondary peaks of the four nuclides, namely  $^{115}\text{In}$ ,  $^{197}\text{Au}$ ,  $^{nat}\text{W}$ , and  $^{nat}\text{Ag}$ . These peaks act as fingerprints to identify the presence of nuclides in the samples. We selected the energy regions with these characteristic peaks for full-image neutron resonance imaging. As shown in Fig. 9, the four samples of  $^{115}\text{In}$ ,  $^{197}\text{Au}$ ,  $^{nat}\text{W}$ , and  $^{nat}\text{Ag}$  can be independently identified using the spatial distribution. Each image was normalized and divided by a background image that selected the non-resonance-energy region adjacent to the dominant peak of the nuclide to represent each nuclide separately. This image processing was discussed in a previous article [17].  $^{115}\text{In}$  and  $^{nat}\text{W}$  can be easily identified owing to their distinct and non-overlapping resonances at approximately 1.4 eV-1.5 eV and 18.0 eV-19.5 eV, respectively. However, the dominant

peaks of the  $^{197}\text{Au}$  and  $^{nat}\text{Ag}$  overlap at approximately 4.5 eV-5.5 eV, which causes them to simultaneously appear during resonance-identification imaging. To distinguish between  $^{197}\text{Au}$  and  $^{nat}\text{Ag}$ , we selected a part of the  $^{197}\text{Au}$  peak at approximately 4.8 eV-5.0 eV to exclude  $^{nat}\text{Ag}$ , as well as the secondary peaks of  $^{nat}\text{Ag}$  at approximately 16.0 eV-16.5 eV. This reduces the image statistics, which can be solved by using longer measurement durations. In the absence of the coexistence of  $^{197}\text{Au}$  and  $^{nat}\text{Ag}$ , the imaging effect using the dominant peaks was better. The nuclides with cross-sectional resonances in the eV energy regions can be easily identified and imaged using the B-MCP detector at the Back-n source with the advantage of strong resonance peaks.

#### B. Nuclides with cross-section resonances in the 1-100 keV regions

Fig. 10 presents the cross-sections of  $^{nat}\text{Cu}$ ,  $^{nat}\text{Fe}$ , and  $^{27}\text{Al}$  over a wide energy range from 100 eV to 500 keV [35]. The resonance peaks were mostly located in this region, and the peak heights were nearly two orders of magnitude lower than those of the heavy elements in Sec. IV A, which complicates nuclide resonance imaging owing to a reduction in the imaging contrast. Moreover, the peaks were significantly narrow, which further reduces the cross-sectional integral. Because the widths of the resonance peaks in this energy region were comparable to the spacing between the two neutron bunches, the pulse structure introduces approximately 14%-50% of the undesired neutrons into the selected resonance ranges [17]. This effect can be resolved with sufficient statistics by using energy-resolved processing, in which the double-bunch structure can still be used to identify these elements by selecting energy-resolved neutrons [36].

Fig. 11a shows the Cu, Fe and Al samples with the same thickness of 10 mm. Fig. 11b shows the neutron transmission image in the full-energy region, in which all the constituents are clearly visible. The Cu and Fe samples exhibited

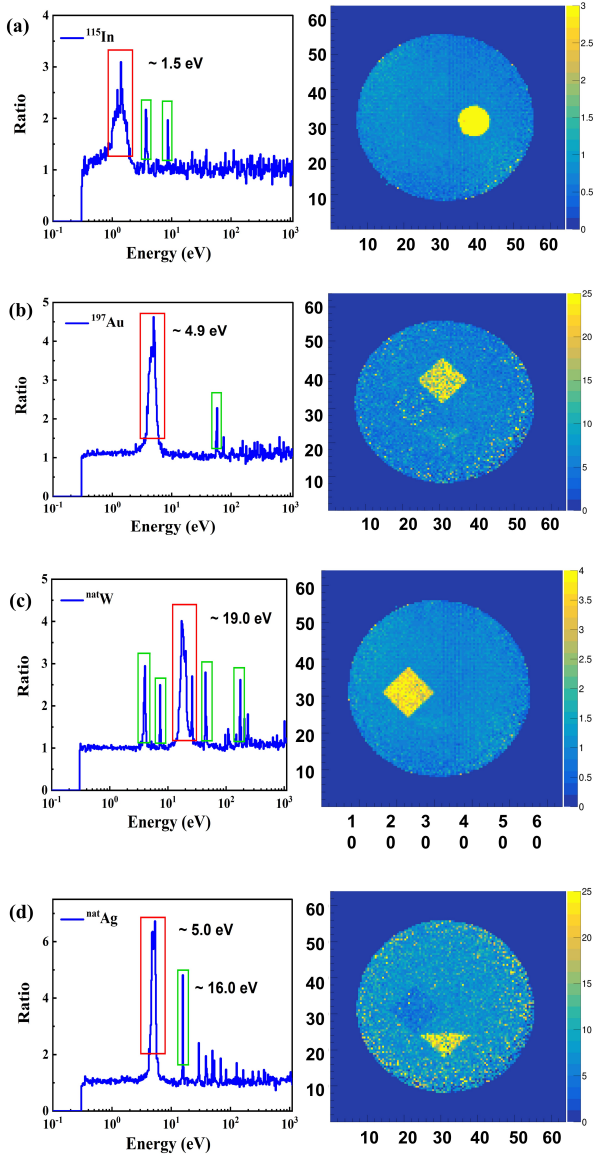


Fig. 9. Identification imaging with the selected energy region corresponding to the resonance peak of (a)  $^{115}\text{In}$ , (b)  $^{197}\text{Au}$ , (c)  $^{\text{nat}}\text{W}$ , and (d)  $^{\text{nat}}\text{Ag}$ .

high and similar brightness values owing to their strong neutron absorption. The Al area is the darkest because its cross-sectional integral over the full-energy region (including the nucleus number density) is smaller than those of Fe and Cu, as illustrated in Fig. 10. As expected, the individual nuclides were unable to be identified via total-transmission imaging.

Resonance imaging analyses were performed to identify the samples and their spatial distribution by using the same method described in Sec. IV A. The ratio spectra with and without the samples in the sample areas are shown in Fig. 12. The peak clusters in the ratio spectra reflect the nuclide species, which sufficiently correspond with the resonances of the sample nuclides  $^{\text{nat}}\text{Cu}$ ,  $^{\text{nat}}\text{Fe}$ , and  $^{27}\text{Al}$ . We selected the energy regions with these characteristic peaks for full-area

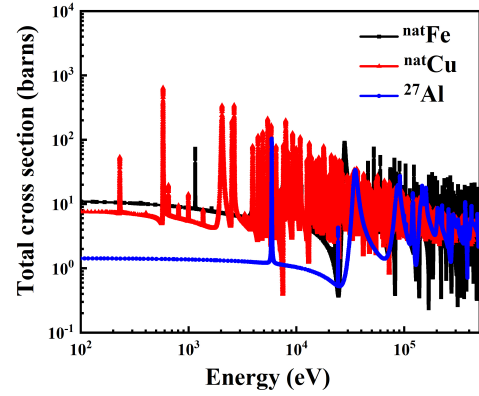


Fig. 10. Neutron cross-sections of  $^{\text{nat}}\text{Cu}$ ,  $^{\text{nat}}\text{Fe}$ , and  $^{27}\text{Al}$  in the energy region of 100 eV–500 keV.

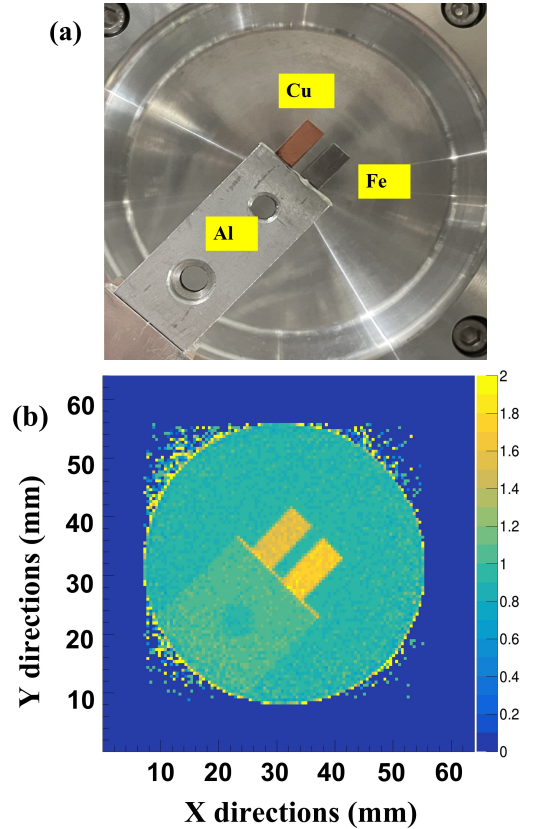


Fig. 11. (a) Sample objects and (b) the neutron transmission image over the full-energy region.

resonance imaging, as shown in Fig. 12. The three samples of Cu, Fe, and Al could be independently identified with a spatial distribution, although not as well as the samples in the eV energy region. This is partly because the intensity and width of these resonances are not large and because the detection efficiency of  $^{10}\text{B}$  in the keV region is reduced. In particular, for the Al sample, the three wider resonances at approxi-



mately 35, 90, and 150 keV were selected instead of the highest resonance. They have a cross-section of only 20 barns, but the signal-to-noise ratio is significantly better than that of a higher but narrow peak. The nuclides with cross-sectional resonances in the keV energy regions can be identified and imaged at the Back-n source with a good signal-to-noise ratio of the B-MCP detector. One advantage of the B-MCP detector over other methods such as the CMOS/CCD camera is that it can simultaneously obtain multiple resonances of nuclides for superimposed imaging to improve the signal-to-noise ratio and resonant image contrast.

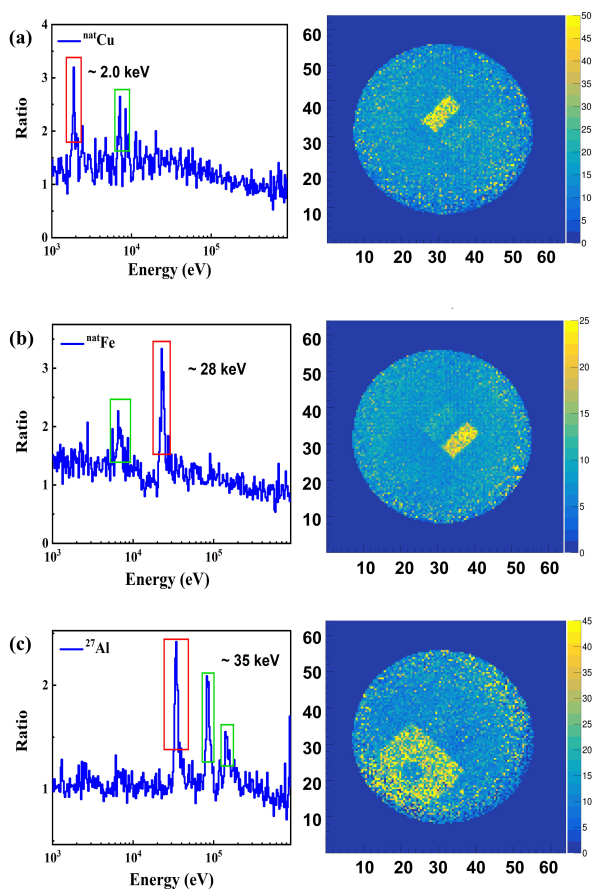


Fig. 12. Identification imaging with the selected energy region corresponding to the resonance peaks of (a)  $^{nat}\text{Cu}$ , (b)  $^{nat}\text{Fe}$ , and (c)  $^{27}\text{Al}$ .

Ideally, B-MCP can provide neutron energy-count spectra

at each pixel for a more detailed imaging analysis, or the charge distribution of each neutron for a higher spatial resolution beyond the strip width. This requires a sufficiently large amount of data with at least one million counts per pixel. Therefore, the detection efficiency of B-MCP is a critical factor for high-quality resonance imaging. A sufficiently large amount of data can also be used to resolve the double-bunch of neutron pulses of Back-n, which is beneficial for the analysis and imaging of nuclides with resonances above keV. Other aspects of the B-MCP that need to be considered include the ratio of the  $n/\gamma$  efficiency, and control of the B-MCP gain, that is, the signal amplitude range. In this study, the images of nuclides with resonances in the keV region demonstrate better results than those used by other methods, such as CMOS/CCD cameras, although the detection efficiency of the developed B-MCP is not sufficiently high. This indicates the great potential of the B-MCP detector for achieving good NRI results for most nuclides in a wide energy region from eV to MeV on a suitable white neutron source.

## V. SUMMARY AND PERSPECTIVES

A B-MCP detector system was successfully developed, which can be used for NRI applications, as well as neutron energy-resolved imaging and spatial-resolved neutron spectrum measurements. The MCP stack with combined B-MCP and conventional MCPs, readout electronics, and data analysis system have been sufficiently working, and a few NRI demonstration experiments were conducted at the Back-n white neutron source. For heavy-element samples such as Au, Ag, In, and W in the 1 eV-100 eV energy region and for medium-element samples such as Cu, Fe, and Al in the 1 eV-100 keV energy region, the experiments achieved a good nuclide identification and imaging resolution of 500  $\mu\text{m}$ . In particular, results related to the neutron energy range of dozens of keV were reported for the first time.

To further expand the NRI technique to the neutron energy range of 100 keV to 10 MeV for identifying light elements, the detection efficiency and readout electronics must be improved to handle narrower peaks and significantly high instantaneous data rates. A higher detection efficiency also facilitates the analysis of sufficient data to obtain a better image resolution by using the center of gravity method; for example, approximately 100  $\mu\text{m}$ , which exceeds the width limit of the anode strips. A new version of the B-MCP detector with a higher  $^{10}\text{B}$  doping and faster electronics is under development.

- 
- [1] G.Y. Chen, R.C. Lanza, Fast neutron resonance radiography for elemental imaging: theory and applications. *IEEE Trans. Nucl. Sci.* **49**, 1919–1924 (2002). [doi:10.1109/TNS.2002.801696](https://doi.org/10.1109/TNS.2002.801696)
  - [2] H. Postma, P. Schillebeeckx, Non-destructive analysis of objects using neutron resonance capture. *J. Radioanal. Nucl. Chem.* **265** 297–302 (2005). <https://doi.org/10.1007/s10967-005-0824-4>
  - [3] D. Perticone, B.W. Blackburn, G.Y. Chen et al., Fast neutron resonance radiography for elemental imaging. *Nucl. Instr. Meth. A.* **922**, 71–75 (2019). <https://doi.org/10.1016/j.nima.2018.12.034>
  - [4] R.O. Nelson, S.C. Vogel, J.F. Hunter et al., Neutron Imaging at LANSCE—From Cold to Ultrafast. *Journal of Imaging* **4**, 45 (2018). <https://doi.org/10.3390/jimaging4020045>

- [5] A.S. Tremsin, J. Rakovan, T. Shinohara et al., Non-Destructive Study of Bulk Crystallinity and Elemental Composition of Natural Gold Single Crystal Samples by Energy Resolved Neutron Imaging. *Scientific Reports* **7**, 40759 (2017). <https://doi.org/10.1038/srep40759>
- [6] A.S. Tremsin, A.S. Losko, S.C. Vogel et al., Non-contact measurement of partial gas pressure and distribution of elemental composition using energy-resolved neutron imaging. *AIP Adv.* **7**, 015315 (2017). <https://doi.org/10.1063/1.4975632>
- [7] A.S. Tremsin, A.E. Craft, G.C. Papaioannou et al., On the possibility to investigate irradiated fuel pins non-destructively by digital neutron radiography with a neutron-sensitive microchannel plate detector with Timepix readout. *Nucl. Instr. Meth. A.* **927**, 109–118 (2019). <https://doi.org/10.1016/j.nima.2019.02.012>
- [8] A.S. Tremsin, A.E. Craft, M.A.M. Bourke et al., Digital neutron and gamma-ray radiography in high radiation environments with an MCP/Timepix detector. *Nucl. Instr. Meth. A.* **902**, 110–116 (2018). <https://doi.org/10.1016/j.nima.2018.05.069>
- [9] A.S. Losko, S.C. Vogel, 3D isotope density measurements by energy-resolved neutron imaging. *Sci. Rep.* **12**, 6648 (2022). <https://doi.org/10.1038/s41598-022-10085-3>
- [10] I. Mor, D. Vartsky, M. Brandis et al., Fast-neutron imaging spectrometer based on liquid scintillator loaded capillaries. *JINST* **7**, C04021 (2012). [doi:10.1088/1748-0221/7/04/C04021](https://doi.org/10.1088/1748-0221/7/04/C04021)
- [11] V. Dangendorf, G. Laczko et al., Detectors for Time-of-Flight Fast-Neutron Radiography: 1. Neutron-Counting Gas Detectors. *Nucl. Instr. Meth. A.* **542**, 197–205 (2005). <https://doi.org/10.1016/j.nima.2005.01.100>
- [12] L.X. Zhang, S.Z. Chen, Z.D. Zhang et al., Resolution analysis of thermal neutron radiography based on accelerator-driven compact neutron source. *Nucl. Sci. Tech.* **34**, 76 (2023). <https://doi.org/10.1007/s41365-023-01227-x>
- [13] K.Q. Gao, H. Yi, Q.M. Zhang et al., First experiment on neutron resonance radiography with a Micromegas detector at the Back-n white neutron source. *JINST* **16**, P02036 (2021). <https://doi.org/10.1088/1748-0221/16/02/P02036>
- [14] X.S. Yan, Y.G. Yang, Q. Li et al., Combined gamma-ray and energy-selective neutron radiography at CSNS. *Nucl. Instr. Meth. A.* **955**, 163200 (2020). <https://doi.org/10.1016/j.nima.2019.163200>
- [15] I. Mor, V. Dangendorf, M. Reginatto et al., Reconstruction of Material Elemental Composition Using Fast Neutron Resonance Radiography. *Physics Procedia* **69**, 304–313 (2015). <https://doi.org/10.1016/j.phpro.2015.07.043>
- [16] D. Vartsky, I. Mor, M.B. Goldberg et al., Novel detectors for fast-neutron resonance radiography. *Nucl. Instr. Meth. A.* **623**, 603–605 (2010). <https://doi.org/10.1016/j.nima.2010.03.084>
- [17] L.J. Wang, Q. Li, J.Y. Tang et al., Experimental studies on nuclide identification radiography with a CMOS camera at Back-n white neutron source. *Nucl. Instr. Meth. A.* **1048**, 167892 (2023). <https://doi.org/10.1016/j.nima.2022.167892>
- [18] J.Q. Yang, J.R. Zhou, L.J. Zhang et al., Efficiency calculation of the nMCP with 10B doping based on mathematical models. *Nuclear Engineering and Technology.* **53**, 2364–2370 (2021). <https://doi.org/10.1016/j.net.2021.01.026>
- [19] Y.M. Wang, Y. Tian, Y.G. Yang et al., Detection efficiency evaluation for a large area neutron sensitive microchannel plate detector. *Chin. Phys. C* **40**, 096004 (2016). [doi:10.1088/1674-1137/40/9/096004](https://doi.org/10.1088/1674-1137/40/9/096004)
- [20] A.S. Tremsin, J.V. Vallerga, Unique capabilities and applications of Microchannel Plate (MCP) detectors with Medipix/Timepix readout. *Radiat. Meas.* **130**, 106228 (2020). <https://doi.org/10.1016/j.radmeas.2019.106228>
- [21] J.Q. Yang, J.R. Zhou, L.J. Zhang et al., Recent measurements at the CSNS towards the construction of a nMCP detector for the energy resolved neutron imaging instrument. *Nucl. Instr. Meth. A.* **1003**, 165322 (2021). <https://doi.org/10.1016/j.nima.2021.165322>
- [22] S. Wang, H. Li, C. Cao et al., Optimal calculation of detection efficiency for thermal neutron sensitive microchannel plate. *Acta Phys. Sin.* **64**, 102801 (2015). [doi:10.7498/aps.64.102801](https://doi.org/10.7498/aps.64.102801)
- [23] K. Watanabe, T. Minniti, W. Kockelmann et al., Characterization of a neutron sensitive MCP/Timepix detector for quantitative image analysis at a pulsed neutron source. *Nucl. Instr. Meth. A.* **861**, 55–63 (2017). [http://dx.doi.org/10.1016/j.nima.2017.04.034](https://doi.org/10.1016/j.nima.2017.04.034)
- [24] A.S. Tremsin, M. Morgano, T. Panzner et al., High resolution neutron imaging capabilities with MCP/Timepix detector at BOA beamline at PSI. *Nucl. Instr. Meth. A.* **7**, 486–493 (2015). <https://doi.org/10.1016/j.nima.2014.09.026>
- [25] G.L. Yang, Z.D. An, W. Jiang et al., Measurement of Br(n, $\gamma$ ) cross sections up to stellar s-process temperatures at the CSNS Back-n. *Nucl. Sci. Tech.* **34**, 180 (2023). <https://doi.org/10.1007/s41365-023-01337-6>
- [26] Z.Z. Ren, Y.W. Yang, Y.H. Chen et al., Measurement of the  $^{232}\text{Th}(n,f)$  cross section in the 1–200 MeV range at the CSNS Back-n. *Nucl. Sci. Tech.* **34**, 115 (2023). <https://doi.org/10.1007/s41365-023-01271-7>
- [27] X.R. Hu, G.T. Fan, W. Jiang et al., Measurements of the  $^{197}\text{Au}(n, \gamma)$  cross section up to 100 keV at the CSNS Back-n facility. *Nucl. Sci. Tech.* **32**, 101 (2021). <https://doi.org/10.1007/s41365-021-00931-w>
- [28] X.Y. Liu, Y.W. Yang, R. Liu et al., Measurement of the neutron total cross section of carbon at the Back-n white neutron beam of CSNS. *Nucl. Sci. Tech.* **30**, 139 (2019). <https://doi.org/10.1007/s41365-019-0660-9>
- [29] L.Y. Zhang, H.T. Jing, J.Y. Tang et al., Design of back-streaming white neutron beam line at CSNS. *Appl. Radiat. Isot.* **132**, 212–221 (2018). <https://doi.org/10.1016/j.apradiso.2017.11.013>
- [30] J.Y. Tang, Q. An, J.B. Bai et al., Back-n white neutron source at CSNS and its applications. *Nucl. Sci. Tech.* **32**, 11 (2021). <https://doi.org/10.1007/s41365-021-00846-6>
- [31] Q. Li, G.Y. Luan, J. Bao et al., The  $^6\text{LiF}$ -silicon detector array developed for real-time neutron monitoring at white neutron beam at CSNS. *Nucl. Instr. Meth. A.* **946**, 162497 (2019). <https://doi.org/10.1016/j.nima.2019.162497>
- [32] Q. Li, H.T. Jing, B. Zhou et al., Neutron and  $\gamma$  background measurements of the experimental halls at the CSNS back-streaming white neutron source. *Nucl. Instr. Meth. A.* **980**, 164506 (2020). <https://doi.org/10.1016/j.nima.2020.164506>
- [33] Z. Chen, Readout electronics for white neutron resonance imaging systems based on Microchannel Plate [D]. Hefei: University of Science and Technology of China, 2022:37-39.
- [34] H.T. Jing, J.Y. Tang, H.Q. Tang et al., Studies of back-streaming white neutrons at CSNS. *Nucl. Instr. Meth. A.* **621**, 91–96 (2010). <https://doi.org/10.1016/j.nima.2010.06.097>
- [35] D.A. Brown, M.B. Chadwick, R. Capote et al., ENDF/B-VIII.0: The 8th Major Release of the Nuclear Reaction Data Library with CIELO-project Cross Sections, New Standards and Thermal Scattering Data. *Nucl. Data Sheets* **148**, 1–142 (2018). <https://doi.org/10.1016/j.nds.2018.02.001>
- [36] T. Kai, F. Maekawa, H. Oshitab et al., Visibility estimation for neutron resonance absorption radiography using a

pulsed neutron source. Physics Procedia **43**, 111–120 (2013).

<https://doi.org/10.1016/j.phpro.2013.03.014>